ASME Journal of Applied Mechanics
Online journal at:
https://asmedigitalcollection.asme.org/appliedmechanics

Nonlinear Mechanical Properties of Irregular Architected Materials

Ruicheng Wang
Department of Advanced Manufacturing and Robotics,
Peking University,
Beijing 100871, China
e-mail: rcwang@stu.pku.edu.cn

Yijie Bian
Smart Manufacturing Thrust,
The Hong Kong University of Science and Technology (Guangzhou),
Nansha, Guangzhou 511400, China
e-mail: ybian189@connect.hkust-gz.edu.cn

Ke Liu[1]
Department of Advanced Manufacturing and Robotics,
Peking University,
Beijing 100871, China
e-mail: LIUKE@PKU.EDU.CN

Architected materials have received increasing attention due to their exotic mechanical properties including ultra-high stiffness-to-weight ratio, strength, energy absorption, and toughness. Typically, their mechanical properties and deformation behavior arise from the periodically tessellated unit cells. Although periodicity in conventional architected materials promises homogeneity and predictability in mechanical behaviors, it imposes a strong restriction on the design space of architected materials. Inspired by biomaterials, aperiodic and disordered designs significantly expand the design space and have been proven effective in controlling and optimizing linear elastic properties. Taking a step further, here we focus on the nonlinear properties of irregular lattice materials under large deformation, including the stress–strain curve and specific energy absorption. Such materials are generated by a nature-inspired virtual growth program that assembles predefined geometric building blocks in a stochastic yet controllable manner. The nonlinear properties are analyzed through quasi-static compression experiments and large-scale numerical simulations. Based on the well-agreed experimental and numerical results, through the lens of machine learning techniques, the nonlinear properties show a strong correlation with the appearance frequency of the building blocks and their local connectivity, regardless of the nondeterministic nature of the microstructures. A practical constitutive model is proposed for future developments such as generative design and engineering application. Our research offers valuable insights and serves as an inspiration for deeper exploration into the intricate structure–property relationships within materials with aperiodic and disordered microstructures. [DOI: 10.1115/1.4067570]

Keywords: architected materials, disordered design, energy absorption, constitutive modeling of materials, mechanical properties of materials

1 Introduction

Architected materials are man-made, structured materials that exhibit properties rarely found in nature [1–4], such as high stiffness-to-weight ratio [5–7], strength [8–11], negative Poisson's ratio [12–15], and outstanding specific energy absorption (SEA) performance [16–18]. Hence, they often serve as functional components in diverse areas including aerospace engineering [19–21], medical engineering [22,23], and automotive industry [24–28]. The conventional design strategy for architected materials is straightforward and can be divided into two steps. First, the geometry of the unit cell must be determined. Subsequently, this unit cell is tessellated in two or three directions to form the material [2,29–31]. For example, face-centered cubic (FCC) [32,33] and body-centered cubic (BCC) [34,35] lattice materials are composed of FCC and BCC unit cells, which mimic the geometry of atom distribution rules found in the Bravais lattice model [36]. Although such periodic microstructures are easy to design and analyze, they occupy a limited design space and offer compromised programmability [37,38].

One of the best solutions is to incorporate irregularity and disorder into the design of architected materials, learning from biomaterials in nature [39]. Such architected materials exhibit unprecedented mechanical properties by disrupting the long-range orderedness [40,41]. For example, hierarchical designs mimicking natural shells and bones could enhance recoverability and structural resilience [42,43]. Inspired by the crystal strengthening mechanism, Pham et al. [41] proposed a design strategy of robust and damage-tolerant 3D architected materials by introducing twin boundaries and precipitated phases. Other design strategies are also proposed by discarding the concept of the unit cell. As an example, the 2D honeycomb materials generated by Voronoi tessellation achieve greater energy absorption behavior as the structural irregularity increases [44]. Architected materials generated by pruning beams in 2D lattice materials encompass a broad range within Young's modulus-density space [45]. Recently, an increasing number of works have focused on the design of irregular architected materials, and progress has been made in understanding the intricate and nonlinear relationships between various aspects of disorderedness and material properties [45–48].

To generate irregular 2D and 3D microstructures, a graph-based virtual growth program is proposed, inspired by the growth of various natural materials [49]. This generative program is based on the automatic assembly of predefined building blocks following certain adjacency rules. This bottom-up design strategy provides a novel perspective of understanding the mechanical properties of

[1]Corresponding author.

Contributed by the Applied Mechanics Division of ASME for publication in the Journal of Applied Mechanics. Manuscript received October 27, 2024; final manuscript received November 23, 2024; published online January 24, 2025. Assoc. Editor: Xiaojia Shelly Zhang.

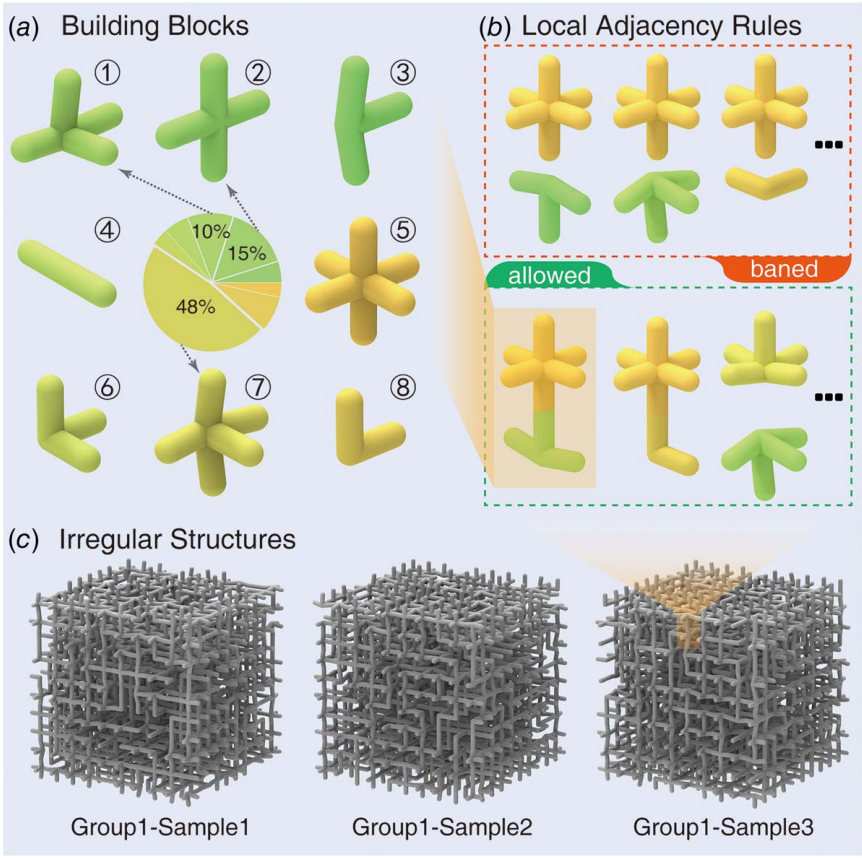

Fig. 1 (*a*) Eight predefined building blocks and their frequencies of appearance to generate group 1 samples, (*b*) local connectivity rules including examples of allowed connections and banned connections, and (c) rendering of three samples of generated irregular lattice materials from group 1

disordered material systems. Many studies have been conducted on such materials [50–52]; however, they mainly focus on the linear elastic properties such as Young's modulus and Poisson ratio. Nonlinear performance such as yield strength and energy absorption has not yet been thoroughly explored [53,54].

In this work, based on the virtual growth program, we study the mechanical properties of irregular lattice materials under large deformation numerically, experimentally, and analytically. The numerical simulations are conducted using the commercial finite element software ABAQUS accelerated by PYTHON scripting. The experimental samples are prepared using the multi jet fusion (MJF) additive manufacturing technology [55]. Furthermore, the Deshpande–Fleck (D–F) model is used to build a constitutive relationship of the irregular lattice materials. Following this introduction, Sec. 2.1 presents the generation process of 3D irregular lattice materials. Section 2.2 describes the setup of the finite element method (FEM) and experiments. The D–F constitutive model utilized in this study is reviewed in Sec. 2.3. The results and discussions are detailed in Sec. 3.1. In Sec. 3.2, we employ the support vector regression (SVR) method to analyze how the local connectivity of building blocks influences the overall properties and deformation patterns of irregular lattice materials [56,57]. Finally, Sec. 4 concludes the study.

2 Methods

2.1 Generation of Irregular Architected Materials. The graph-based virtual growth program [49] is used to generate irregular lattice materials by mimicking the growth of irregular structures in nature [58]. In the generation process, the full design area is first pixelated into grids. The grids are to be filled with predefined building blocks. During the generation process, several constraints should be satisfied, including the lowest entropy rule and local connectivity rule. The lowest entropy rule prevents the random placement of building blocks by introducing each grid with a magnitude of entropy S. S describes how many nearby grids have been filled at the current iteration and is defined as

$$S_i = \sum_{i \in \alpha} -P_i \log P_i \tag{1}$$

where α is the set of admissible building blocks, and P_i denotes the prescribed frequencies of building blocks, which is normalized such that $\sum_i P_i = 1$. In each iteration, we select the grid with minimal entropy to fill with a random building block with the restriction of the local connectivity rule. The local connectivity rule determines pair-wise compatibility, which is defined to ensure good connections between neighboring building blocks and avoid the formation of detached subregions. Once a grid is filled, only compatible building blocks can be assigned to its nearby grids. This prevents the formation of unwanted local structures. The target appearance probability of each building block (the frequency of the building blocks in this work) is achieved through nonuniform random selection. This iterative process runs until all grids are filled.

Using the previously described virtual growth program, we first define eight beam-based building blocks, as shown in Fig. 1(*a*), namely "Branch," "Plus," "T," "Stick," "Cross," "Corner," "Protrusion," and "L," respectively. Each beam element in these building blocks features a radius of 0.8 mm. The dimensions of each building block are 5 mm × 5 mm × 5 mm. Each building block is allowed to rotate and reflect with respect to the X, Y, and Z axes with equal probabilities. As each material sample contains a 10 × 10 × 10 cubic

Table 1 The prescribed and resultant building block frequencies of two example groups

Building blocks	Branch	Plus	T	Stick	Cross	Corner	Protrusion	L
Group 1 (prescribed) (%)	9.8	15.4	4.9	6.6	4.0	4.5	45.7	9.1
Group 1 (resultant) (%)	10.7	15.1	4.9	5.9	3.4	4	47.7	8.3
	9.4	16.3	5.3	7.1	4.7	5.2	43.5	8.5
	7.9	15.2	4.7	6.6	4.3	4.2	49.7	7.4
Group 2 (prescribed) (%)	11.2	28.5	14.3	8	6.8	10	20	1.2
Group 2 (resultant) (%)	10.7	28.5	13.3	7.9	8.2	10.4	19.9	1.1
	10.9	29	12.3	8	5.9	12.2	20.7	1
	1.3	28.9	14.6	7	8.6	8.7	20.9	1

grid of building blocks, the resultant lattice materials' bulk mechanical properties converge to cubic symmetry. We generate 40 groups, each created from different frequencies of building blocks, as shown in Table 1. Each group contains 10 irregular lattice material samples. Due to the restriction of local connectivity rules, the resultant building block frequencies are slightly different from the prescribed values.

2.2 Simulation and Experimental Methods. The mechanical behavior of irregular lattice materials is analyzed through the finite element method (FEM). Next, the quasi-static loading experiments are conducted to validate the accuracy of the numerical results.

2.2.1 Simulation. The commercial software ABAQUS/EXPLICIT in conjunction with PYTHON scripts is used to perform the simulation. Beam element B31 with two nodes based on the Timoshenko hypothesis is used to model the beams in irregular lattice materials. Two rigid plates are applied on the top and bottom to compress the sample, as shown in Fig. 2(*a*). The top plate serves as the loading plate, where all degrees of freedom are constrained except for the *Z*-direction. The bottom plate is the supporting plate with all displacements restricted. The constitutive relation of the constituent material is determined using tensile tests on dog-bone specimens. The dog-bone specimens are printed in the same process and batch as the irregular lattice material samples. According to the tensile stress–strain curve, the elastic modulus E_s and yield stress σ_{ys} are fitted to be 1451.24 MPa and 25.17 MPa, respectively, using the elastoplastic constitutive model. In addition, the Poisson's ratio ν is 0.33 and the density of the material is 1010 kg/m^3. The normal contact behavior is considered as hard contact, and the tangential friction coefficient is set as 0.3. The simulation settings illustrated above are executed using PYTHON script and parallel computing is employed on a supercomputer to save computational time.

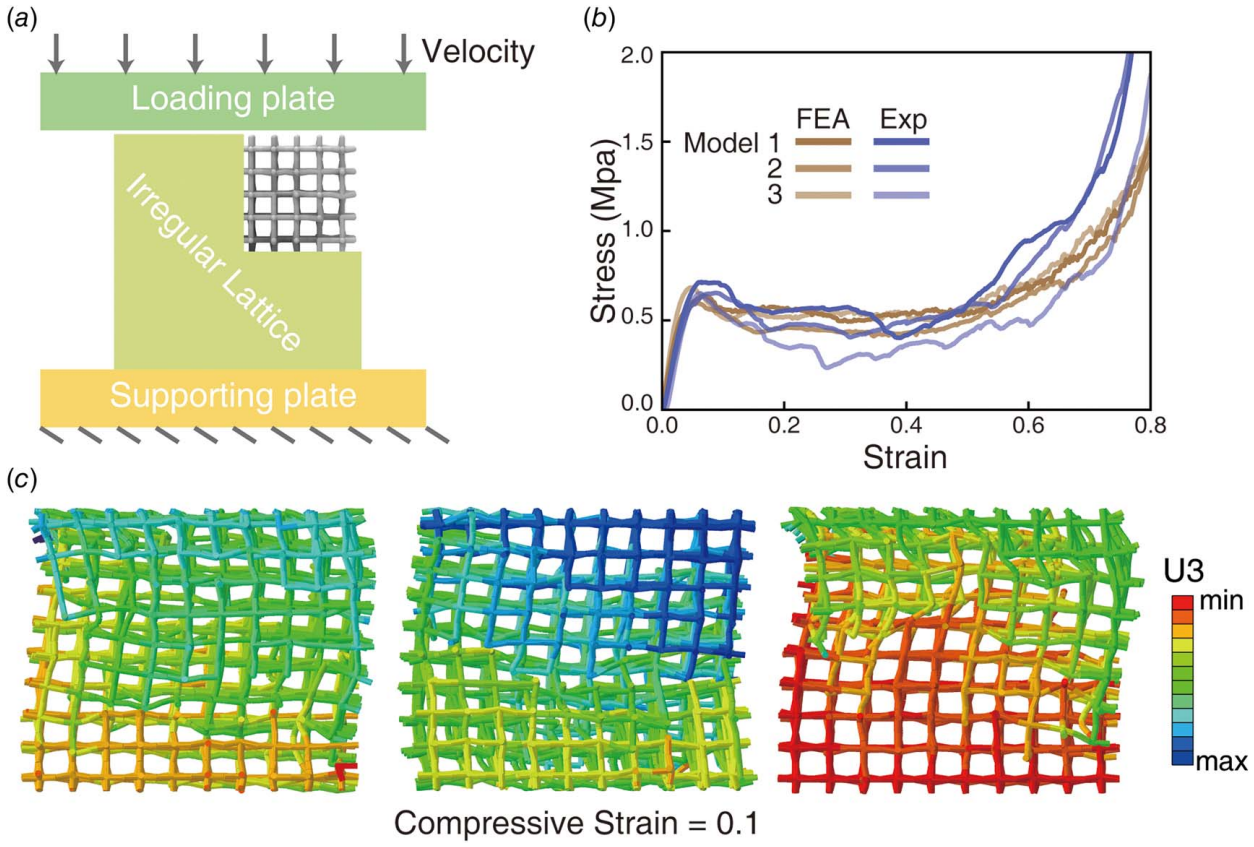

Fig. 2 (*a*) Boundary conditions used in numerical simulation, (*b*) three examples of the comparison of stress–strain curves obtained from FEM and experiments, and (*c*) cloud figures of three samples of group 1 in terms of *Z*-axis displacement under compression strain at 0.1

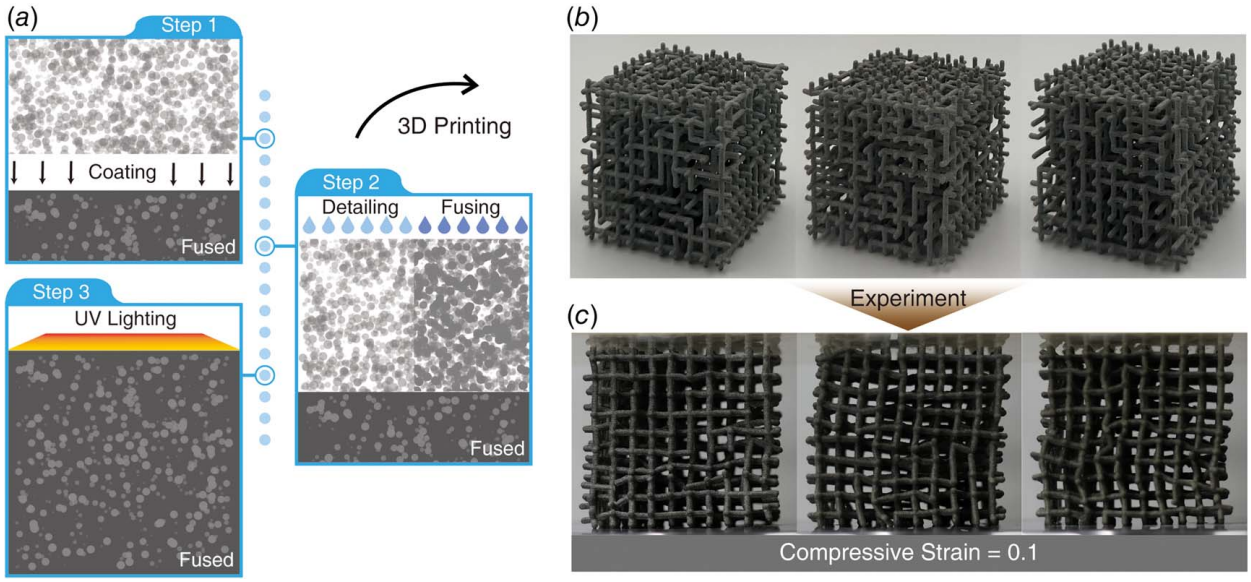

Fig. 3 (*a*) Printing process of the multi jet fusion technology, (*b*) pictures of three printed samples from group 1, and (c) the deformation of these samples under compression

2.2.2 Fabrication and Experiment. In order to validate the credibility of the results from FEM, we physically fabricate 20 models and test them under quasi-static compression for comparison. We use the MJF additive manufacturing technology for fabrication. This technology eliminates the need for complicated support structures and offers high manufacturing efficiency as well as excellent printing quality. The working principle of MJF is illustrated in Fig. 3(*a*). The printing process can be divided into three steps. First, the roller spreads a thin layer of raw powder on the preprinted part. Then a print head comes to the area beyond the new layer and selectively deposits fusing agents onto specific areas of the powder bed corresponding to the part's cross section. Third, an infrared light source passes over the bed, heating the areas with the fusing agents and causing the powder to fuse into solid layers. This sequence is repeated layer by layer until the whole model is built. Three pictures of printed samples are shown in Fig. 3(*b*).

Quasi-static compression experiments are conducted using a universal testing machine (Instron 3366, USA). The specimens are placed on the supporting plate while the loading plate moves downward at a speed of 0.6 mm/min to achieve the quasi-static loading condition. The force–displacement curves are obtained from the tests. Furthermore, the stress is calculated by dividing the force by the gross cross-sectional area (50 mm × 50 mm) and the strain is calculated by dividing the displacement by the height of the sample (50 mm).

2.3 Constitutive Modeling. Several approaches have been proposed to model the nonlinear behaviors of architected materials [59–62]. Particularly, based on a series of experimental observations of metal foams, Deshpande and Fleck proposed several isotropic constitutive models, including the self-similar model and the differential hardening model [63]. Due to its simplicity, the self-similar isotropic constitutive model is popular for modeling a variety of architected materials [64–66]. Considering the structural similarity between metal foam and irregular lattice materials, in this work, the self-similar D–F model is used to characterize the constitutive relation of irregular lattice materials based on uniaxial compression data. This model provides a practical approach to describe the homogenized behavior of irregular lattice materials for future applications.

In the self-similar D–F model, the formula of yield function is assumed as

$$\Phi \equiv \hat{\sigma} - Y = 0 \tag{2}$$

where $\hat{\sigma}$ is the equivalent stress, defined as

$$\hat{\sigma} \equiv \frac{\sigma_e^2 + \alpha^2 \sigma_m^2}{1 + (\alpha/3)^2} \tag{3}$$

In this expression, Y is the yield stress, and σ_m and σ_e represent the mean and effective stress, respectively. The effective stress can be expressed using Einstein's summation convention as follows:

$$\sigma_m = \frac{\sigma_{kk}}{3} \tag{4}$$

$$\sigma_e = \sqrt{\frac{3}{2} S_{ij} : S_{ij}} \tag{5}$$

where S_{ij} is the stress deviator.

In addition, α represents the shape of the yield surface. The model assumes that the ellipticity remains constant in the subsequent yield and its magnitude is dependent on plastic Poisson's ratio:

$$\alpha^2 = \frac{9(1 - 2\nu^p)}{2(1 + \nu^p)} \tag{6}$$

The post-yielding correlation can be further expressed. The effective strain rate is given by

$$\dot{\varepsilon}_{ij}^p = \frac{1}{H} \frac{\partial \Phi}{\partial \sigma_{ij}} \frac{\partial \Phi}{\partial \sigma_{kl}} \check{\sigma}_{kl} \tag{7}$$

where H is the hardening coefficient defined by Eq. (10) and $\check{\sigma}_{kl}$ is the Jaumann rate. This formula can be simplified by defining von Mises's effective plastic strain rate and the volumetric plastic strain rate as

$$\dot{\varepsilon}_e \equiv \sqrt{\frac{2}{3} \dot{\varepsilon}_{ij}^p \dot{\varepsilon}_{ij}^p} = \frac{\dot{\hat{\varepsilon}}}{[1 + (\alpha/3)^2]} \frac{\sigma_e}{\hat{\sigma}} \tag{8}$$

$$\dot{\varepsilon}_m \equiv \dot{\varepsilon}_{kk}^p = \frac{\alpha^2 \dot{\hat{\varepsilon}}}{[1 + (\alpha/3)^2]} \frac{\sigma_m}{\hat{\sigma}} \tag{9}$$

$$H(\hat{\varepsilon}) = \frac{\dot{\sigma}_{33}}{\dot{\varepsilon}^p_{33}} \tag{10}$$

Then substituting Eqs. (8) and (9) into the expression of equivalent stress, we obtain

$$\dot{\hat{\varepsilon}}^2 = \left[1 + \left(\frac{\alpha}{3}\right)^2\right]\left(\dot{\varepsilon}_e^2 + \frac{1}{\alpha^2}\dot{\varepsilon}_m^2\right) \tag{11}$$

Finally, the plastic strain rate is [67]

$$\dot{\varepsilon}^p_{ij} = \dot{\hat{\varepsilon}}\frac{\partial \Phi}{\partial \sigma_{ij}} = \frac{\dot{\hat{\varepsilon}}}{1 + (\alpha/3)^2}\left(\frac{3}{2}\frac{S_{ij}}{\hat{\sigma}} + \frac{\alpha^2}{3}\delta_{ij}\frac{\sigma_m}{\hat{\sigma}}\right) \tag{12}$$

where δ_{ij} is the Kronecker delta.

3 Results and Discussion

3.1 Results. We extract the mechanical properties, including stiffness, strength, and energy absorption, from the obtained stress–strain curves in numerical simulations and experiments. The comparisons and analyses focus on specific properties, including the specific elastic modulus (SEM), specific strength (SS), and SEA, calculated by dividing the equivalent density of the samples. The definitions of strength and energy absorption are detailed as follows.

The strength of irregular lattice materials is defined as the maximum stress between the strain 0 and 0.1, which refers to either the peak stress or the stress magnitude at the strain of 0.1. The energy absorption capacity of the irregular lattice materials is calculated by Eq. (13), where ε_d is the densification strain determined by the peak value of the energy absorption efficiency (EAE). EAE is defined as $\eta = EA/\sigma_p$, with σ_p being the peak stress during the compression [68]. Additionally, the plateau stress of the lattice is calculated using Eq. (14), where ε_y denotes the initial yield strain.

$$EA = \int_0^{\varepsilon_d} \sigma(\varepsilon)\mathrm{d}\varepsilon \tag{13}$$

$$\sigma_{pl} = \frac{\int_{\varepsilon_y}^{\varepsilon_d} \sigma(\varepsilon)\mathrm{d}\varepsilon}{\varepsilon_d - \varepsilon_y} \tag{14}$$

3.1.1 Comparison Between Simulation and Experimental Results. The comparison of stress–strain curves of three samples in group 1 between the simulated and experimental results is shown in Fig. 2(*b*). The comparisons of other samples are shown in Fig. 9 in the Appendix. These curves show a high degree of agreement. A slight deviation is observed near the densification stage, owing to internal contact in the physical models [69]. Their deformation behavior under numerical and physical tests is shown in Figs. 2(*c*) and 3(*c*). Furthermore, the mechanical properties, including SEM, SS, and SEA, are captured and compared with numerical results, showing average errors of 13.48%, 16%, and 15.51%, respectively (see Tables 2 and 3 in the Appendix). This result shows that our FEM model is credible for large-scale calculations, and future analyses will primarily rely on these simulation results.

3.1.2 The Convergence of Properties Under Large Deformation. We compare the average mechanical properties under large deformation among different groups, each generated with a different setup of building block frequencies. Within each group, although the generating building block frequencies remain the same, the actual structure of each sample is different from one another due to the randomness during the virtual growth process. The Ashby plot in terms of specific stiffness and plateau stress of six groups is shown in Fig. 4(*a*). The results show that in the same group, the stress–strain curves remain substantially similar for all samples. In contrast, the stress–strain curves between

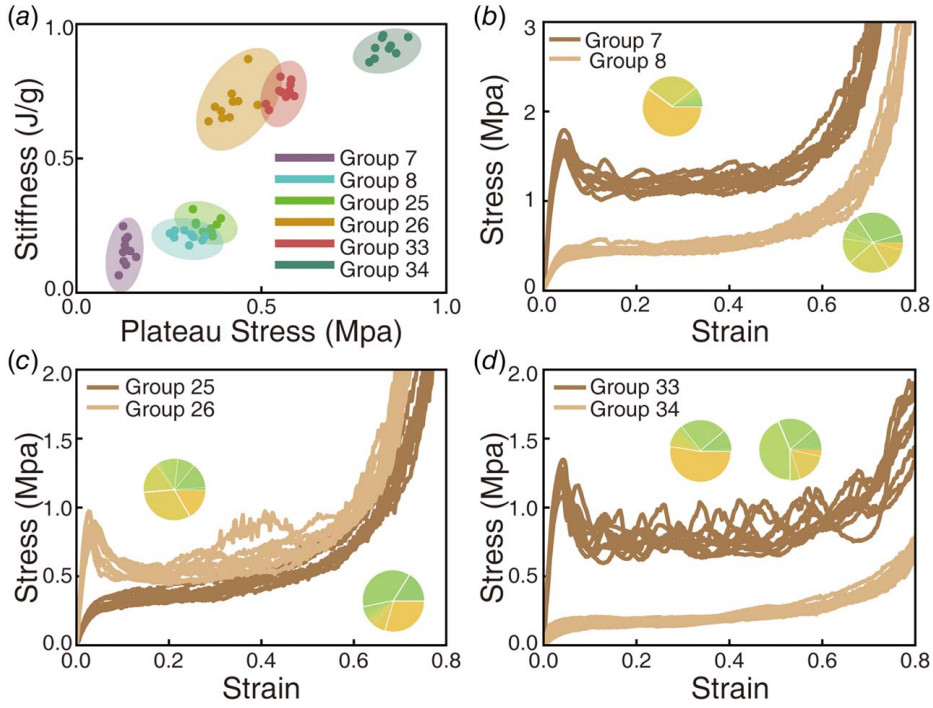

Fig. 4 (*a*) Ashby plot with respect to specific stiffness and plateau stress, showing data from six representative sample groups. (*b*)–(*d*) The stress–strain curves of samples in the six groups. The pie plots represent the frequencies of building blocks, as explained in Fig. 1(*a*).

different groups become notably different, as shown in Figs. 4(*b*)–4(*d*). For example, the plateau stresses of samples in group 7 are much higher than those in group 8. In addition, the group 7 samples exhibit obvious peak values after the initial linear stage, exhibiting the typical loading curve of stretch-dominated lattice (type II structure as defined in Ref. [70]). In contrast, the loading curves of the group 8 samples show the characteristics of the bending-dominated lattice (type I structure in Ref. [70]), with a smooth transition between the initial linear stage and plateau stage. Group 25 and group 26 demonstrate similar plateau stresses, but all group 26 samples show obvious peak stresses after the initial linear stage. The observation is that the group 25 samples are rich in building block "L," while the group 26 samples have more building block "Plus" and block "Cross." The building block frequencies have a notable effect on the nonlinear mechanical properties and large deformation behavior of the irregular lattice materials.

The compressive deformation of periodic lattices usually concentrates in certain patterned regions, such as the shear bands observed in many architected materials [37]. However, different from the layer-by-layer crush observed in the periodic lattices, irregular lattice materials exhibit a more uniform deformation, as shown in Fig. 2(*c*). This may be because the nonuniformity of irregular lattice materials provides extensive paths of stress percolation. Hence, beams with maximum stress will appear uniformly throughout the whole structure rather than in specific regions. The irregular lattice materials seem to enhance the mechanical integrity and robustness of the lattice materials.

As discussed above, in irregular lattice material systems, by varying the frequencies of building blocks, the structural type and deformation mode change accordingly. Figure 5(*a*) shows two samples with different building block frequencies exhibiting different deformation modes: stretching-dominated and bending-dominated modes, respectively. For the stretching-dominated sample, at the peak stress, many beams undergo sudden buckling, causing a noticeable stress drop in the stress–strain curve. However, no peak stress occurs in the bending-dominated sample, as most beams undergo gradual bending. We observe that buckling often happens where two building blocks are connected, rather than within a single building block, which indicates that the frequency of building block pairs also plays an important role in the nonlinear deformation behavior of irregular lattice materials.

We propose a new approach to distinguish bending or stretching-dominated structures. Here, we reduce the dimensionality of the frequencies of building block pairs between the eight basic building blocks into a two-dimensional visible plane using principal component analysis (PCA). As shown in Fig. 5(*b*), the two types of structures can be separated clearly. It is observed that the deformation mode depends more on dimension PCA1. The right plot shows that there are four building block pairs that contribute most to PCA1, including pairs "Cross-Cross," "Cross-Protrusion," "Cross-Branch," and "Cross-Plus." In particular, increasing the proportion of these four pairs will transfer the structure from bending-dominated to stretching-dominated. As a result, the deformation mode of irregular lattice materials could be tuned by controlling

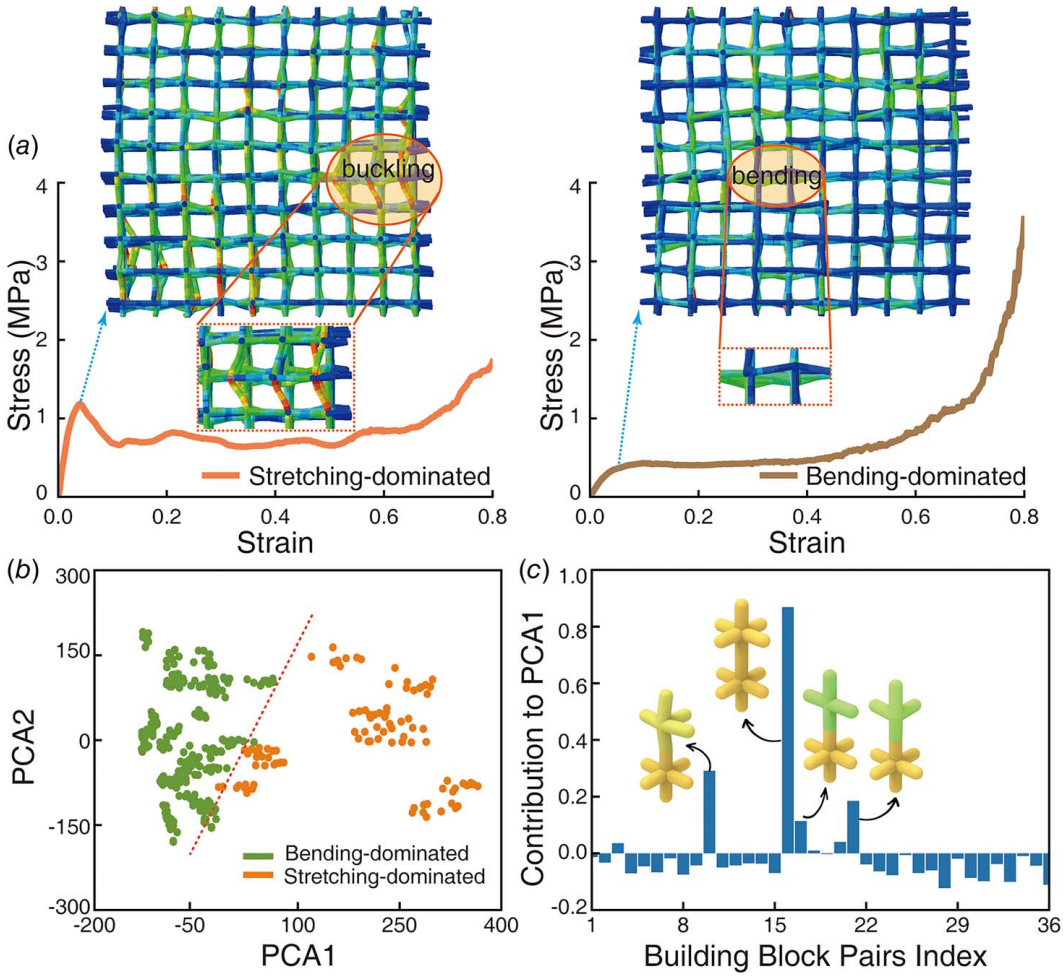

Fig. 5 (*a*) Compression behavior of stretching-dominated versus bending-dominated irregular lattice materials, (*b*) two-dimensional plot of the two primary components from PCA of building block pair frequencies, and (*c*) contribution of building block pairs to PCA1

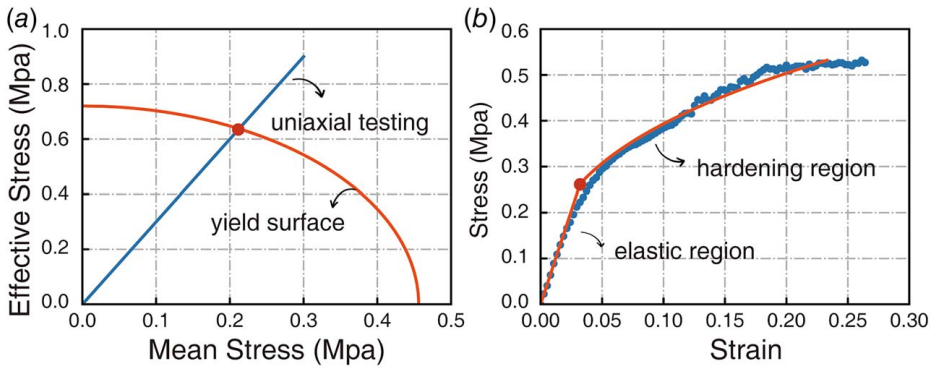

Fig. 6 (*a*) The fitted initial yield surface of an example structure. The straight line is the result of uniaxial compression with a slope of 1/3 and the elliptic curve is the shape of the initial yield surface. (*b*) The fitted stress–strain curve under uniaxial compression of the same sample. The dots represent the simulated data and the solid line represents the fitted curve.

the frequencies of specific building block pairs. The building block pairs' contribution to PCA2 is shown in Fig. 10 of the Appendix.

3.1.3 Initial Yield Surface Using the D–F Model. We use the self-similar D–F model to fit the function of the initial yield surface. In this study, we use 1.58 as a reasonable value for α based on previous research about open foams [71]. The fitted yield surface is shown as the red line in Fig. 6(*a*). The blue line represents the result of uniaxial compression from FEM with a slope of 1/3, which is defined as

$$\frac{\sigma_m}{\sigma_e} = \frac{1}{3} \tag{15}$$

3.1.4 Uniaxial Compression Stress–Strain Relation. The relation between stress and strain under uniaxial compression can be fitted by assuming the curve shape as [67]

$$\varepsilon = \begin{cases} \sigma/E, & \sigma \le \sigma_y \\ \varepsilon_y(\sigma/\sigma_y)^{1/N}, & \sigma > \sigma_y \end{cases} \tag{16}$$

where σ_y and ε_y are the yield stress and yield strain, and N is the strain hardening coefficient. One of the examples is shown in Fig. 6(*b*). The blue dots represent the simulated data and the red line represents the fitted curve. Among the irregular lattice materials, the magnitude of N varies from 0.06 to 1.12, as the frequencies of building blocks change. The influences of Block "Corner" and Block "T" on the strain hardening coefficient are shown in Fig. 7. A clear negative correlation is observed between the frequency of Block "Corner" and N, while a positive correlation is noted regarding Block "T."

3.2 Supporting Vector Regression Analysis. As discussed above, the mechanical properties of irregular lattice materials rely on the frequencies of both building blocks and building block pairs. We use the support vector regression (SVR) [72] method to build the relationship between frequency parameters and the properties. The SVR analysis aims to find a few hyperplanes that can effectively divide data in high-dimensional space. It captures the underlying patterns and correlations, enabling accurate predictions regarding nonlinear relationships.

We first preprocess the simulated data, including data standardization, handling missing values, and splitting the preprocessed dataset into training and testing sets with a ratio of 20%. After data preprocessing, we select the radial basis function as the kernel for its advantage of capturing nonlinear relationships. To optimize the model's performance, we conduct a grid search over key SVR parameters, such as the regularization parameter C and the kernel parameter γ, using five-fold cross-validation to evaluate the effectiveness of different parameter combinations. The performance of the best-trained model is evaluated using the coefficient of determination R^2, as shown in Fig. 8(*a*). By using the frequencies of building block pairs as the input, the results show that the SVR model can effectively and accurately capture the nonlinear characteristics of irregular lattice materials.

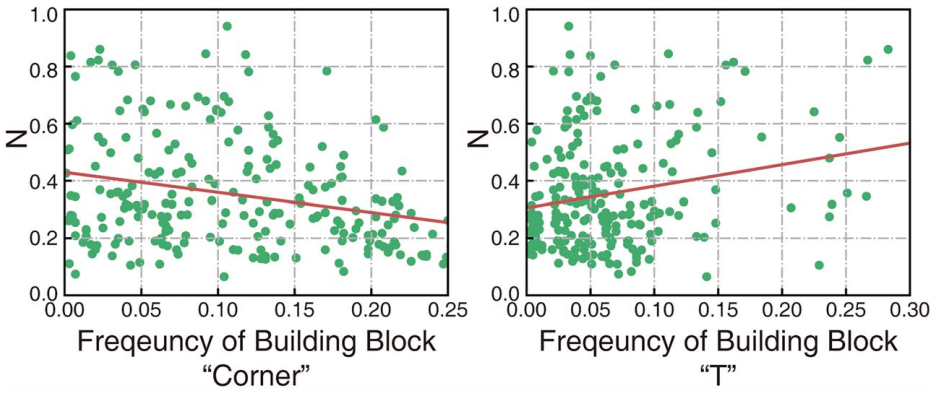

Fig. 7 The influence of frequencies of Block "Corner" and "T" on the strain hardening coefficient *N*. The solid lines are fitted using the least-squares regression method to show the correlation between frequencies of building blocks and *N*. The negative and positive correlations are shown regarding Block "Corner" and Block "T," respectively.

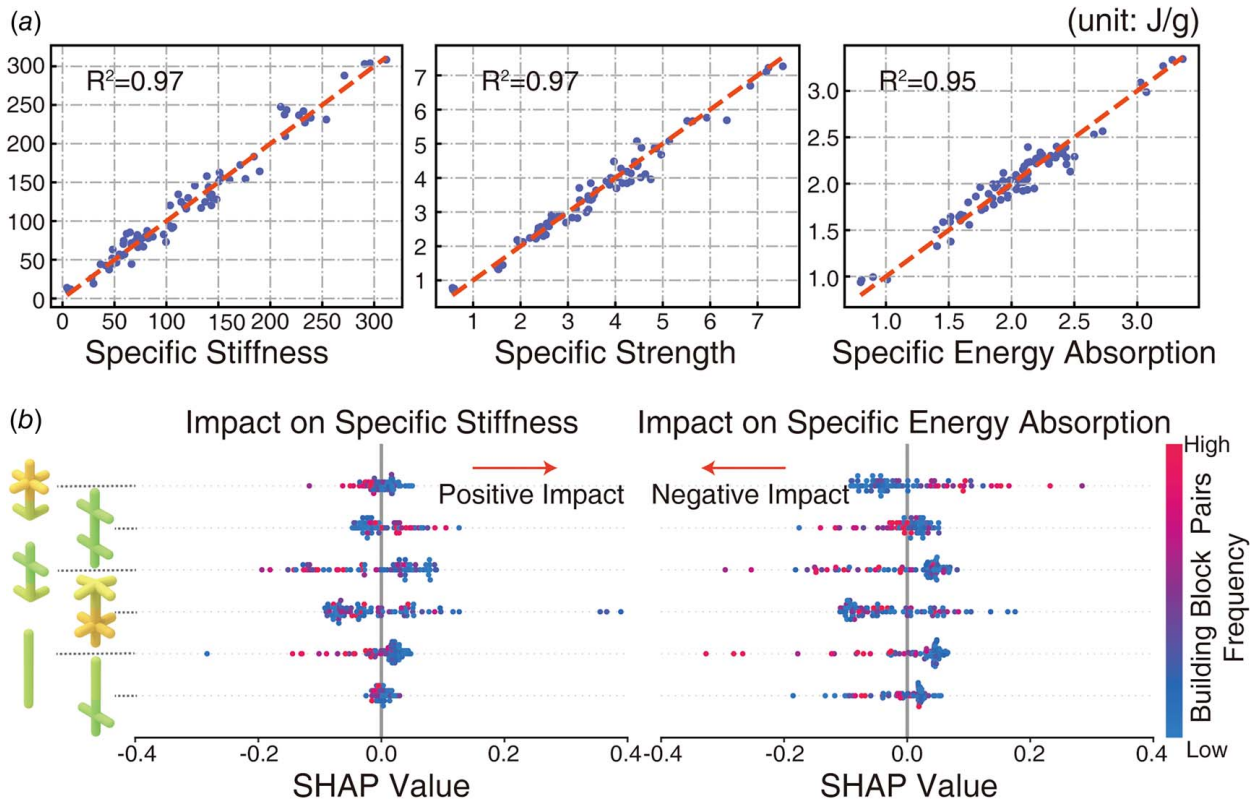

Fig. 8 (*a*) Coefficient of determination of the trained SVR model on the testing dataset, considering both building blocks and building block pairs level, and (*b*) SHAP analysis of the impact of building block pairs frequencies on specific properties including stiffness and energy absorption

We further analyze the impact of building block pair frequencies on the specific properties, including stiffness and energy absorption, using the Shapley Additive exPlanations (SHAP) tool [73]. This technique has been widely used for the interpretation of machine learning model regressions. As seen in Fig. 8(*b*), pairs "Plus-Corner," "Protrusion-Cross," and "Stick-Stick" have similar influence trends on both properties, which means the two properties could be enhanced accordingly by controlling the frequencies of these building block pairs. However, pairs "Cross-Corner" and "Plus-Plus" have the opposite influence on linear property and nonlinear energy absorption. Strengthening one of the behaviors by adjusting these building block pairs will lead to a decrease in the other one. One can also see the amounts of pair "Stick-Plus" significantly influence the structures' specific energy absorption capacity, but will not cause an obvious change in specific stiffness. The SVR model combined with SHAP analysis provides a reliable approach to examine the correlation between the frequency of building blocks (and building block pairs) and mechanical properties.

4 Concluding Remarks

In this work, we utilize the virtual growth program to create a variety of irregular lattice materials controlled by the frequencies of predefined building blocks. We conduct extensive FEM, validated by experiments on 3D printed samples using multi jet fusion technology. We fit a self-similar Deshpande–Fleck constitutive model to approximate the constitutive behavior of the irregular lattice materials. In addition, we employ principal component analysis and support vector regression to analyze how building block and building block pair frequencies influence the overall mechanical properties and deformation mode. Our main conclusions are listed below:

(1) Irregular lattice materials generated using the same frequencies of building blocks exhibit converging mechanical properties, including specific stiffness, specific strength, and specific energy absorption. Those with different frequencies behave drastically differently.
(2) By controlling the frequencies of building blocks, the deformation mode of the irregular lattice materials divides into either stretching-dominated or bending-dominated. In addition to building block frequencies, we observe that the frequencies of building block pairs also play a vital role in determining the characteristics of global compression behavior.
(3) The trained SVR model combined with SHAP analysis provides an accurate prediction from frequencies of building blocks to property space. Such machine learning tools provide useful guidance for designing new architected materials and tuning their mechanical properties.

Acknowledgment

This research is supported by the National Natural Science Foundation of China through grant 12372159 and the National Key Research and Development Program of China through grant 2022YFB4701900.

Conflict of Interest

There are no conflicts of interest.

Data Availability Statement

The datasets generated and supporting the findings of this article are obtainable from the corresponding author upon reasonable request.

Appendix

Table 2 Comparison of mechanical properties between experiments and simulations in terms of SEM, SS, and SEA

	SEM (J/g)			SS (J/g)			SEA (J/g)		
Sample	Exp	FEM	Error	Exp	FEM	Error	Exp	FEM	Error
1_1	114.194	117.605	2.900%	3.623	4.484	19.198%	2.011	1.857	7.653%
1_2	111.723	105.713	5.379%	3.445	4.016	14.202%	1.926	1.747	9.261%
1_3	138.414	121.668	12.098%	3.862	4.190	7.823%	1.924	1.702	11.529%
2_1	149.452	100.502	32.753%	3.744	3.043	18.721%	1.858	1.302	29.917%
2_2	114.906	107.544	6.407%	3.339	3.905	14.510%	1.695	1.713	1.092%
2_3	157.023	145.584	7.285%	3.792	4.418	14.175%	1.890	1.968	4.000%
3_1	198.244	196.330	0.965%	5.082	6.598	22.972%	2.659	2.669	0.391%
3_2	201.389	125.811	37.528%	5.371	4.247	20.928%	2.702	1.735	35.785%
3_3	174.994	145.251	16.997%	4.264	4.865	12.350%	2.458	2.963	17.044%
4_1	259.799	213.423	17.851%	5.399	6.650	18.816%	2.629	2.824	6.889%
4_2	323.087	252.617	21.812%	6.177	7.067	12.595%	2.949	2.970	0.706%
4_3	291.791	224.842	22.944%	5.768	6.462	10.742%	2.650	2.040	22.991%
5_1	177.571	174.161	1.920%	4.333	6.439	32.703%	2.168	3.243	33.148%
5_2	149.436	138.115	7.576%	3.769	4.725	20.248%	2.940	4.081	27.955%
5_3	187.804	168.062	10.512%	4.574	5.543	17.471%	2.755	3.144	12.359%
6_1	133.973	121.724	9.143%	3.716	3.956	6.053%	1.936	2.049	5.511%
6_2	111.313	102.869	7.585%	3.404	3.515	3.166%	2.577	1.656	35.735%
6_3	129.792	87.585	32.519%	3.518	2.243	36.253%	1.597	1.153	27.826%

Table 3 Comparison of mechanical properties between experiments and simulations in terms of plateau stress and densification strain

	Plateau stress (MPa)			Densification strain		
Sample	Exp	FEM	Error	Exp	FEM	Error
1_1	0.565	0.546	3.446%	0.637	0.544	14.637%
1_2	0.499	0.507	1.582%	0.672	0.566	15.829%
1_3	0.558	0.399	28.512%	0.616	0.651	5.349%
2_1	0.475	0.297	37.382%	0.645	0.622	3.597%
2_2	0.438	0.495	11.525%	0.629	0.533	15.358%
2_3	0.478	0.478	0.085%	0.651	0.631	3.072%
3_1	0.749	0.554	26.064%	0.704	0.787	10.526%
3_2	0.761	0.398	47.678%	0.696	0.682	2.016%
3_3	0.785	0.749	4.656%	0.629	0.707	10.964%
4_1	0.612	0.653	6.334%	0.736	0.681	7.447%
4_2	0.666	0.717	7.054%	0.800	0.703	12.149%
4_3	0.612	0.406	33.682%	0.744	0.754	1.304%
5_1	0.756	0.984	23.216%	0.579	0.615	5.880%
5_2	0.817	1.031	20.836%	0.728	0.745	2.237%
5_3	0.849	0.765	9.894%	0.667	0.733	9.012%
6_1	0.518	0.481	7.059%	0.611	0.640	4.563%
6_2	0.630	0.416	33.932%	0.699	0.597	14.509%
6_3	0.472	0.260	45.017%	0.555	0.611	9.195%

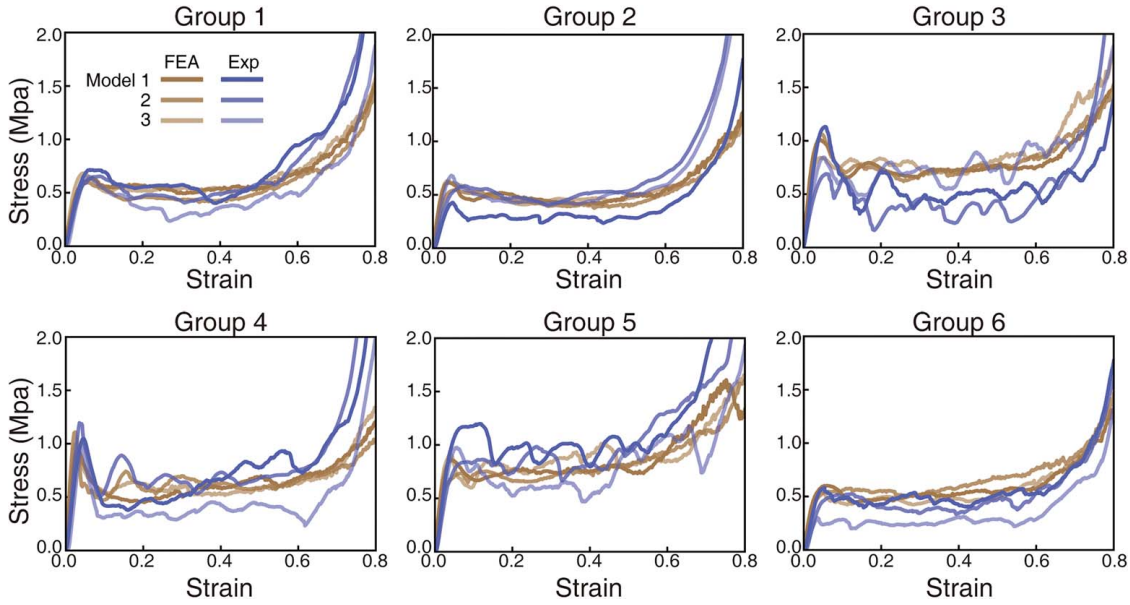

Fig. 9 The comparisons of samples' stress–strain curves between experiments and simulations

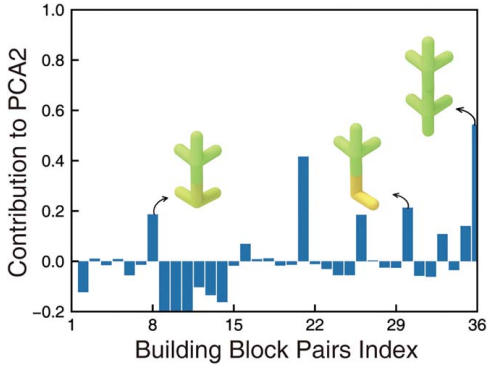

Fig. 10 The building block pairs contribution to the PCA2, discussed in Sec. 3.1.2

References

[1] Xia, X., Spadaccini, C. M., and Greer, J. R., 2022, "Responsive Materials Architected in Space and Time," Nat. Rev. Mater., **7**(9), pp. 683–701.

[2] Deshpande, V. S., Fleck, N. A., and Ashby, M. F., 2001, "Effective Properties of the Octet-Truss Lattice Material," J. Mech. Phys. Solids, **49**(8), pp. 1747–1769.

[3] Wang, L., Chang, Y., Wu, S., Zhao, R. R., and Chen, W., 2023, "Physics-Aware Differentiable Design of Magnetically Actuated Kirigami for Shape Morphing," Nat. Commun., **14**(1), p. 8516.

[4] Bessa, M. A., Glowacki, P., and Houlder, M., 2019, "Bayesian Machine Learning in Metamaterial Design: Fragile Becomes Supercompressible," Adv. Mater., **31**(48), p. 1904845.

[5] Zheng, X., Lee, H., Weisgraber, T. H., Shusteff, M., DeOtte, J., Duoss, E. B., Kuntz, J. D., et al., 2014, "Ultralight, Ultrastiff Mechanical Metamaterials," Science, **344**(6190), pp. 1373–1377.

[6] Wang, F., Brøns, M., and Sigmund, O., 2023, "Non-hierarchical Architected Materials With Extreme Stiffness and Strength," Adv. Funct. Mater., **33**(13), p. 2211561.

[7] Mueller, J., Raney, J. R., Shea, K., and Lewis, J. A., 2018, "Architected Lattices With High Stiffness and Toughness Via Multicore-Shell 3D Printing," Adv. Mater., **30**(12), p. 1705001.

[8] Bauer, J., Schroer, A., Schwaiger, R., and Kraft, O., 2016, "Approaching Theoretical Strength in Glassy Carbon Nanolattices," Nat. Mater., **15**(4), pp. 438–443.

[9] Li, T., Jarrar, F., Al-Rub, R. A., and Cantwell, W., 2021, "Additive Manufactured Semi-Plate Lattice Materials With High Stiffness, Strength and Toughness," Int. J. Solids Struct., **230**, p. 111153.

[10] Wang, Y., Zhang, X., Li, Z., Gao, H., and Li, X., 2022, "Achieving the Theoretical Limit of Strength in Shell-Based Carbon Nanolattices," Proc. Natl. Acad. Sci. USA, **119**(34), p. e2119536119.

[11] Gu, X. W., and Greer, J. R., 2015, "Ultra-strong Architected Cu Meso-lattices," Extreme Mech. Lett., **2**, pp. 7–14.

[12] Lakes, R., 1987, "Foam Structures With a Negative Poisson's Ratio," Science, **235**(4792), pp. 1038–1040.

[13] Baughman, R. H., Shacklette, J. M., Zakhidov, A. A., and Stafström, S., 1998, "Negative Poisson's Ratios as a Common Feature of Cubic Metals," Nature, **392**(6674), pp. 362–365.

[14] Xu, N., Liu, H.-T., An, M.-R., and Wang, L., 2021, "Novel 2D Star-Shaped Honeycombs With Enhanced Effective Young's Modulus and Negative Poisson's Ratio," Extreme Mech. Lett., **43**, p. 101164.

[15] Zheng, B., and Gu, G. X., 2019, "Tuning the Graphene Mechanical Anisotropy Via Defect Engineering," Carbon, **155**, pp. 697–705.

[16] Wang, P., Yang, F., Li, P., Zheng, B., and Fan, H., 2021, "Design and Additive Manufacturing of a Modified Face-Centered Cubic Lattice With Enhanced Energy Absorption Capability," Extreme Mech. Lett., **47**, p. 101358.

[17] Cheng, H., Zhu, X., Cheng, X., Cai, P., Liu, J., Yao, H., Zhang, L., and Duan, J., 2023, "Mechanical Metamaterials Made of Freestanding Quasi-BCC Nanolattices of Gold and Copper With Ultra-high Energy Absorption Capacity," Nat. Commun., **14**(1), p. 1243.

[18] Li, X., Yu, X., Chua, J. W., Lee, H. P., Ding, J., and Zhai, W., 2021, "Microlattice Metamaterials With Simultaneous Superior Acoustic and Mechanical Energy Absorption," Small, **17**(24), p. 2100336.

[19] Schaedler, T. A., Jacobsen, A. J., Torrents, A., Sorensen, A. E., Lian, J., Greer, J. R., Valdevit, L., and Carter, W. B., 2011, "Ultralight Metallic Microlattices," Science, **334**(6058), pp. 962–965.

[20] Vasiliev, V. V., Barynin, V. A., and Razin, A. F., 2012, "Anisogrid Composite Lattice Structures—Development and Aerospace Applications," Compos. Struct., **94**(3), pp. 1117–1127.

[21] Antimirova, E., Jung, J., Zhang, Z., Machuca, A., and Gu, G. X., 2024, "Overview of Computational Methods to Predict Flutter in Aircraft," ASME J. Appl. Mech., **91**(5), p. 050801.

[22] Lvov, V. A., Senatov, F. S., Veveris, A. A., Skrybykina, V. A., and Díaz Lantada, A., 2022, "Auxetic Metamaterials for Biomedical Devices: Current Situation, Main Challenges, and Research Trends," Materials, **15**(4), p. 1439.

[23] McGregor, M., Patel, S., McLachlin, S., and Vlasea, M., 2021, "Architectural Bone Parameters and the Relationship to Titanium Lattice Design for Powder Bed Fusion Additive Manufacturing," Addit. Manuf., **47**, p. 102273.

[24] Cui, H., Yao, D., Hensleigh, R., Lu, H., Calderon, A., Xu, Z., Davaria, S., et al., 2022, "Design and Printing of Proprioceptive Three-Dimensional Architected Robotic Metamaterials," Science, **376**(6599), pp. 1287–1293.

[25] Lee, R. H., Mulder, E. A., and Hopkins, J. B., 2022, "Mechanical Neural Networks: Architected Materials That Learn Behaviors," Sci. Rob., **7**(71), p. eabq7278.

[26] Wen, L., Pan, F., and Ding, X., 2020, "Tensegrity Metamaterials for Soft Robotics," Sci. Rob., **5**(45), p. eabd9158.

[27] Chen, T., Pauly, M., and Reis, P. M., 2021, "A Reprogrammable Mechanical Metamaterial With Stable Memory," Nature, **589**(7842), pp. 386–390.

[28] Chen, T., Bilal, O. R., Lang, R., Daraio, C., and Shea, K., 2019, "Autonomous Deployment of a Solar Panel Using Elastic Origami and Distributed Shape-Memory-Polymer Actuators," Phys. Rev. Appl., **11**(6), p. 064069.

[29] Fleck, N. A., Deshpande, V. S., and Ashby, M. F., 2010, "Micro-architectured Materials: Past, Present and Future," Proc. R. Soc. A: Math. Phys. Eng. Sci., **466**(2121), pp. 2495–2516.

[30] Chen, X., Moughames, J., Ji, Q., Martínez, J. A. I., Tan, H., Adrar, S., Laforge, N., et al., 2020, "Optimal Isotropic, Reusable Truss Lattice Material With Near-Zero Poisson's Ratio," Extreme Mech. Lett., **41**, p. 101048.

[31] Zhang, W., Yang, W., Zhou, J., Li, D., and Guo, X., 2017, "Structural Topology Optimization Through Explicit Boundary Evolution," ASME J. Appl. Mech., **84**(1), p. 011011.

[32] Lee, K.-W., Lee, S.-H., Noh, K.-H., Park, J.-Y., Cho, Y.-J., and Kim, S.-H., 2019, "Theoretical and Numerical Analysis of the Mechanical Responses of BCC and FCC Lattice Structures," J. Mech. Sci. Technol., **33**(5), pp. 2259–2266.

[33] Jin, N., Yan, Z., Wang, Y., Cheng, H., and Zhang, H., 2021, "Effects of Heat Treatment on Microstructure and Mechanical Properties of Selective Laser Melted Ti-6Al-4V Lattice Materials," Int. J. Mech. Sci., **190**, p. 106042.

[34] Liu, Y., Zhang, J., Gu, X., Zhou, Y., Yin, Y., Tan, Q., Li, M., and Zhang, M.-X., 2020, "Mechanical Performance of a Node Reinforced Body-Centred Cubic Lattice Structure Manufactured Via Selective Laser Melting," Scr. Mater., **189**, pp. 95–100.

[35] Liu, X., Kobir, M. H., Yang, Y., Jiang, F., and Kothari, T., 2023, "Improving Stiffness and Strength of Body-Centered Cubic Lattices With an I-Shape Beam Cross-section," Mech. Mater., **182**, p. 104665.

[36] Kittel, C., 2005, *Introduction to Solid State Physics, 8th Edition*, John Wiley & Sons, Hoboken, NJ.

[37] Li, W., Fan, H., Bian, Y., and Yang, F., 2021, "Plastic Deformation and Energy Absorption of Polycrystalline-Like Lattice Structures," Mater. Des., **198**, p. 109321.

[38] Lei, H., Li, C., Zhang, X., Wang, P., Zhou, H., Zhao, Z., and Fang, D., 2021, "Deformation Behavior of Heterogeneous Multi-morphology Lattice Core Hybrid Structures," Addit. Manuf., **37**, p. 101674.

[39] Zaiser, M., and Zapperi, S., 2023, "Disordered Mechanical Metamaterials," Nat. Rev. Phys., **5**(11), pp. 679–688.

[40] Giménez-Ribes, G., Motaghian, M., van der Linden, E., and Habibi, M., 2023, "Crumpled Structures as Robust Disordered Mechanical Metamaterials," Mater. Des., **232**, p. 112159.

[41] Pham, M.-S., Liu, C., Todd, I., and Lertthanasarn, J., 2019, "Damage-Tolerant Architected Materials Inspired by Crystal Microstructure," Nature, **565**(7739), pp. 305–311.

[42] Meza, L. R., Zelhofer, A. J., Clarke, N., Mateos, A. J., Kochmann, D. M., and Greer, J. R., 2015, "Resilient 3D Hierarchical Architected Metamaterials," Proc. Natl. Acad. Sci. USA, **112**(37), pp. 11502–11507.

[43] Zheng, X., Smith, W., Jackson, J., Moran, B., Cui, H., Chen, D., Ye, J., et al., 2016, "Multiscale Metallic Metamaterials," Nat. Mater., **15**(10), pp. 1100–1106.

[44] Zheng, Z., Yu, J., and Li, J., 2005, "Dynamic Crushing of 2D Cellular Structures: A Finite Element Study," Int. J. Impact Eng., **32**(1–4), pp. 650–664.

[45] Rayneau-Kirkhope, D., Bonfanti, S., and Zapperi, S., 2019, "Density Scaling in the Mechanics of a Disordered Mechanical Meta-material," Appl. Phys. Lett., **114**(11), p. 111902.

[46] Aage, N., Andreassen, E., Lazarov, B. S., and Sigmund, O., 2017, "Giga-Voxel Computational Morphogenesis for Structural Design," Nature, **550**(7674), pp. 84–86.

[47] Hanifpour, M., Petersen, C. F., Alava, M. J., and Zapperi, S., 2018, "Mechanics of Disordered Auxetic Metamaterials," Eur. Phys. J. B, **91**(11), pp. 1–8.

[48] Bonfanti, S., Guerra, R., Font-Clos, F., Rayneau-Kirkhope, D., and Zapperi, S., 2020, "Automatic Design of Mechanical Metamaterial Actuators," Nat. Commun., **11**(1), p. 4162.

[49] Liu, K., Sun, R., and Daraio, C., 2022, "Growth Rules for Irregular Architected Materials With Programmable Properties," Science, **377**(6609), pp. 975–981.

[50] Liu, Y., Xia, B., Liu, K., Zhou, Y., and Wei, K., 2024, "Robustness and Diversity of Disordered Structures on Sound Absorption and Deformation Resistance," J. Mech. Phys. Solids, **190**, p. 105751.

[51] Jia, Y., Liu, K., and Zhang, X. S., 2024, "Modulate Stress Distribution With Bio-inspired Irregular Architected Materials Towards Optimal Tissue Support," Nat. Commun., **15**(1), p. 4072.

[52] Jia, Y., Liu, K., and Zhang, X. S., 2024, "Topology Optimization of Irregular Multiscale Structures With Tunable Responses Using a Virtual Growth Rule," Comput. Methods Appl. Mech. Eng., **425**, p. 116864.

[53] Magrini, T., Fox, C., Wihardja, A., Kolli, A., and Daraio, C., 2024, "Control of Mechanical and Fracture Properties in Two-Phase Materials Reinforced by Continuous, Irregular Networks," Adv. Mater., **36**(6), p. 2305198.
[54] Fox, C., Chen, K., Antonini, M., Magrini, T., and Daraio, C., 2024, "Extracting Geometry and Topology of Orange Pericarps for the Design of Bioinspired Energy Absorbing Materials," Adv. Mater., **36**(36), p. 2405567.
[55] Cai, C., Tey, W. S., Chen, J., Zhu, W., Liu, X., Liu, T., Zhao, L., and Zhou, K., 2021, "Comparative Study on 3D Printing of Polyamide 12 by Selective Laser Sintering and Multi Jet Fusion," J. Mater. Process. Technol., **288**, p. 116882.
[56] Lee, D., Chen, W., Wang, L., Chan, Y. C., and Chen, W., 2024, "Data-Driven Design for Metamaterials and Multiscale Systems: A Review," Adv. Mater., **36**(8), p. 2305254.
[57] Olatunji, S. O., 2021, "Modeling Optical Energy Gap of Strontium Titanate Multifunctional Semiconductor Using Stepwise Regression and Genetic Algorithm Based Support Vector Regression," Comput. Mater. Sci., **200**, p. 110797.
[58] Huiskes, R., 2000, "If Bone Is the Answer, Then What Is the Question?," J. Anat., **197**(2), pp. 145–156.
[59] Rusch, K., 1969, "Load–Compression Behavior of Flexible Foams," J. Appl. Polym. Sci., **13**(11), pp. 2297–2311.
[60] Hanssen, A., Hopperstad, O. S., Langseth, M., and Ilstad, H., 2002, "Validation of Constitutive Models Applicable to Aluminium Foams," Int. J. Mech. Sci., **44**(2), pp. 359–406.
[61] Avalle, M., Belingardi, G., and Ibba, A., 2007, "Mechanical Models of Cellular Solids: Parameters Identification From Experimental Tests," Int. J. Impact Eng., **34**(1), pp. 3–27.
[62] Ashby, M.F., and Gibson, L.J., 1997, *Cellular Solids: Structure and Properties*, Press Syndicate University of Cambridge, Cambridge, UK, pp. 175–231.
[63] Deshpande, V. S., and Fleck, N. A., 2000, "Isotropic Constitutive Models for Metallic Foams," J. Mech. Phys. Solids, **48**(6–7), pp. 1253–1283.
[64] Khaderi, S. N., Scherer, M., Hall, C., Steiner, U., Ramamurty, U., Fleck, N., and Deshpande, V., 2017, "The Indentation Response of Nickel Nano Double Gyroid Lattices," Extreme Mech. Lett., **10**, pp. 15–23.
[65] Guo, X., Wang, E., Yang, H., and Zhai, W., 2024, "Mechanical Characterization and Constitutive Modeling of Additively-Manufactured Polymeric Materials and Lattice Structures," J. Mech. Phys. Solids, **189**, p. 105711.
[66] Babamiri, B. B., Askari, H., and Hazeli, K., 2020, "Deformation Mechanisms and Post-Yielding Behavior of Additively Manufactured Lattice Structures," Mater. Des., **188**, p. 108443.
[67] Chen, C., Fleck, N. A., and Lu, T. J., 2001, "The Mode I Crack Growth Resistance of Metallic Foams," J. Mech. Phys. Solids, **49**(2), pp. 231–259.
[68] San Ha, N., and Lu, G., 2020, "A Review of Recent Research on Bio-inspired Structures and Materials for Energy Absorption Applications," Composites Part B, **181**, p. 107496.
[69] He, Z., Wang, F., Zhu, Y., Wu, H., and Park, H. S., 2017, "Mechanical Properties of Copper Octet-Truss Nanolattices," J. Mech. Phys. Solids, **101**, pp. 133–149.
[70] Calladine, C., and English, R., 1984, "Strain-Rate and Inertia Effects in the Collapse of Two Types of Energy-Absorbing Structure," Int. J. Mech. Sci., **26**(11–12), pp. 689–701.
[71] Gioux, G., McCormack, T., and Gibson, L. J., 2000, "Failure of Aluminum Foams Under Multiaxial Loads," Int. J. Mech. Sci., **42**(6), pp. 1097–1117.
[72] Cerniauskas, G., Sadia, H., and Alam, P., 2024, "Machine Intelligence in Metamaterials Design: A Review," Oxford Open Mater. Sci., **4**(1), p. itae001.
[73] Lundberg, S. M., and Lee, S.-I., 2017, "A Unified Approach to Interpreting Model Predictions," NIPS'17: Proceedings of the 31st International Conference on Neural Information Processing Systems 30, Long Beach CA, Dec. 4–9.